which is essentially just a two-dimensional interface. The lack of basaltic meteorites with a $\Delta^{17}O$ value equivalent to the main-group pallasites suggests that the outer crustal layers were removed from the parent asteroid. This may have taken place during the pallasite-forming impact event itself. If loss of surface material took place as the result of a collisional encounter (*24*), the extent of silicate loss appears to have been much less in the pallasites than mesosiderites, because the former show no evidence for remelting of the metal core.

Metal in main-group pallasites is compositionally similar to that in the IIIAB irons, such that both groups are probably derived from the same asteroid (*26*). W isotope dating of IIIAB irons indicates that the metal-silicate segregation event that formed them occurred extremely early (<1 My after Solar System formation) (*3*). Mn-Cr dating is consistent with an early formation age for main-group pallasites (*10*), although the isotope systematics show evidence of disturbance, probably in part as a consequence of impact-related processes (*27*). The cooling rates recorded by main-group pallasites also reflect impact-related processes. Thus, cooling at high temperatures (~1100°C) took place 10^6 times faster than at lower temperatures (~1°C/My at 800° to 400°C) (*27*). The higher rates may have resulted from impact-driven mixing of partially molten metal and solid silicate mantle material, whereas slower cooling may reflect postimpact burial (*25*).

The results presented here demonstrate that pallasites and mesosiderites are derived from distinct asteroidal sources. Like the HEDs, mesosiderites are probably samples from the asteroid 4 Vesta, a conclusion that can be tested by the NASA Dawn Mission (*21*). It is also clear from these results that extensive asteroidal deformation was an important process during the early stages of planetary formation. Recent observations suggest that such collisional reprocessing of planetesimals may also be a significant feature of extrasolar planetary systems, such as the solar-type star BD+20 307 (*28*).

References and Notes

1. S. J. Weidenschilling, *Space Sci. Rev.* **92**, 295 (2000).
2. D. C. Rubie, C. K. Gessmann, D. J. Frost, *Nature* **429**, 58 (2004).
3. A. Markowski, G. Quitté, A. N. Halliday, T. Kleine, *Earth Planet. Sci. Lett.* **242**, 1 (2006).
4. M. Bizzarro, J. A. Baker, H. Haack, K. L. Lundgaard, *Astrophys. J.* **632**, L41 (2005).
5. T. H. Burbine, T. J. McCoy, A. Meibom, B. Gladman, K. Keil, in *Asteroids III*, W. F. Bottke Jr., A. Cellino, P. Paolicchi, R. P. Binzel, Eds. (Univ. Arizona Press, Tucson, AZ, 2002), pp. 653–667.
6. R. N. Clayton, T. K. Mayeda, *Geochim. Cosmochim. Acta* **60**, 1999 (1996).
7. R. C. Greenwood, I. A. Franchi, A. Jambon, P. C. Buchanan, *Nature* **435**, 916 (2005).
8. Oxygen has three naturally occurring stable isotopes, ^{16}O, ^{17}O, and ^{18}O, with natural abundances of ~99.762%, 0.038%, and 0.200%, respectively (*29*). Oxygen isotope variation is reported in terms of per mil (‰) differences in the ratios $^{18}O/^{16}O$ and $^{17}O/^{16}O$ relative to the VSMOW (Vienna Standard Mean Ocean Water) standard expressed as $\delta^{18}O = [(^{18}O/^{16}O)_{sample}/(^{18}O/^{16}O)_{VSMOW}) - 1]1000$ and similarly for $\delta^{17}O$ using $^{17}O/^{16}O$ ratio of the sample and VSMOW. Oxygen isotope values are conventionally plotted on a "three-isotope plot" with $\delta^{18}O$ along the *x* axis and $\delta^{17}O$ along the *y* axis. On such a plot, rocks and waters on Earth define a single line with a slope close to 0.52, known as the terrestrial fractionation line. Deviations from this line are conventionally expressed as: $\Delta^{17}O = \delta^{17}O - 0.52\ \delta^{18}O$; however, this is in fact an approximation of a power law function, and hence the more accurate linearized format is used here: $\Delta^{17}O = 1000\ \ln[1+(\delta^{17}O/1000)] - \lambda 1000\ \ln[1+(\delta^{18}O/1000)]$, where $\lambda = 0.5247$ (*29*).
9. Main-group pallasites and mesosiderites are composed of subequal amounts of Fe-Ni metal and silicate material. The two groups are texturally and compositionally quite distinct. Main-group pallasites consist of large olivine crystals enclosed in Fe-Ni metal, whereas mesosiderites are complex breccias of metal-rich clasts, basaltic, gabbroic, and rarer pyroxenitic fragments enclosed in a fine-grained metal-silicate matrix. HEDs are a suite of basaltic and related coarser-grained igneous meteorites that are believed to be samples of the outer crust of asteroid 4 Vesta (*10*).
10. D. W. Mittlefehldt, T. J. McCoy, C. A. Goodrich, A. Kracher, in *Planetary Materials*, J. J. Papike, Ed. (*Min. Soc. Am. Reviews in Mineralogy* 36), 4-1 (1998).
11. T. H. Burbine *et al.*, *Meteorit. Planet. Sci.* **36**, 761 (2001).
12. M. F. Miller, I. A. Franchi, A. S. Sexton, C. T. Pillinger, *Rapid Commun. Mass Spectrom.* **13**, 1211 (1999).
13. Materials and methods are available as supporting material on *Science* Online.
14. U. Wiechert, A. N. Halliday, H. Palme, D. Rumble, *Earth Planet. Sci. Lett.* **221**, 373 (2004).
15. R. H. Hewins, *J. Geophys. Res.* **88** (Supplement), B257 (1983).
16. A. H. Rubin, D. W. Mittlefehldt, *Icarus* **101**, 201 (1993).
17. M. T. Rosing, H. Haack, *Lunar Planet. Sci. Conf.* **35**, 1487 (2004).
18. A. Yamaguchi, C. Okamoto, M. Ebihara, *Lunar Planet. Sci. Conf.* **37**, 1678 (2006).
19. The following olivine-rich diogenites have been identified in recent years: GRA 98108, NWA 1459, NWA 1877, NWA 2629, and NWA 2286. Details of each of these specimens is available on the Meteoritical Bulletin Database, http://tin.er.usgs.gov/meteor.
20. M. Wadhwa, A. Shukolyukov, A. M. Davis, G. W. Lugmair, D. W. Mittlefehldt, *Geochim. Cosmochim. Acta* **67**, 5047 (2003).
21. C. T. Russell *et al.*, *Planet. Space Sci.* **52**, 465 (2004).
22. J. T. Wasson, A. E. Rubin, *Nature* **318**, 168 (1985).
23. R. D. Scott, H. Haack, S. G. Love, *Meteorit. Planet. Sci.* **36**, 869 (2001).
24. E. Asphaug, C. B. Agnor, Q. Williams, *Nature* **439**, 155 (2006).
25. E. R. D. Scott, G. J. Taylor, *Lunar Planet. Sci. Conf.* **21**, 1119 (1990).
26. J. T. Wasson, B.-G. Choi, *Geochim. Cosmochim. Acta* **67**, 3079 (2003).
27. T. Tomiyama, G. R. Huss, *Lunar Planet. Sci. Conf.* **36**, 2071 (2005).
28. I. Song, B. Zuckerman, A. J. Weinberger, E. E. Becklin, *Nature* **436**, 363 (2005).
29. M. F. Miller, *Geochim. Cosmochim. Acta* **66**, 1881 (2002).

30. We would like to thank M. Farmer, who supplied samples of Dong Ujimqin QI; B. Zanda (Muséum National d'Histoire Naturelle, Paris) and C. Smith (Natural History Museum, London) for providing mesosiderite and pallasite samples; and Jenny Gibson (Open University) for help with various aspects of oxygen isotope analysis. We would like to thank three anonymous reviewers for their comments. This study was supported by a PPARC rolling grant to PSSRI, Open University. T.H.B. acknowledges support from NASA Cosmochemistry grant NAG5-12848.

Supporting Online Material

www.sciencemag.org/cgi/content/full/1128865/DC1
Materials and Methods
Figs. S1 and S2
Table S1

18 April 2006; accepted 27 July 2006
Published online 24 August 2006;
10.1126/science.1128865
Include this information when citing this paper.

Self-Healing Pulse-Like Shear Ruptures in the Laboratory

George Lykotrafitis, Ares J. Rosakis,* Guruswami Ravichandran

Models predict that dynamic shear ruptures during earthquake faulting occur as either sliding cracks, where a large section of the interface slides behind a fast-moving rupture front, or self-healing slip pulses, where the fault relocks shortly behind the rupture front. We report experimental visualizations of crack-like, pulse-like, and mixed rupture modes propagating along frictionally held, "incoherent" interfaces separating identical solids, and we describe the conditions under which those modes develop. A combination of simultaneously performed measurements via dynamic photoelasticity and laser interferometry reveals the rupture mode type, the exact point of rupture initiation, the sliding velocity history, and the rupture propagation speed.

A central issue in the modeling of earthquake rupture is the duration of slip at a point on the fault as compared to the duration of the rupture of the entire fault (*1*). In the classical crack-like mode of shear rupture (*2*), the slip duration at a point (rise time) is a considerable fraction of the overall rupture propagation time. In other words, the duration of the ground shaking, witnessed locally by an observer, is comparable to the overall duration of the earthquake. This mode has been generated in several numerical simulations of spontaneous rupture, when a rate-independent friction law was implemented (*3*–*7*). However, inversions of seismic data for slip histories from well-recorded events indicate that the duration of slip at a point on the fault is often one order of magnitude shorter

Graduate Aeronautical Laboratories, California Institute of Technology, Pasadena, CA 91125, USA.

*To whom correspondence should be addressed. E-mail: Rosakis@aero.caltech.edu

than the event duration (*8*–*10*). This observation has led to the concept of pulse-like rupture modes (*8*, *11*), in which the slip is confined to a finite distance behind the propagating rupture front while the fault continuously locks.

Various mechanisms for self-healing pulse generation along a homogeneous fault have been proposed. One such mechanism suggests that if the fault strength is low immediately behind the rupture front and if it increases rapidly at a finite distance, resulting in a robust join between the contacting surfaces, then the slip would be restricted to a short and narrow propagating area (*12*). For example, a strong velocity-weakening friction law model (that is, the fault strength drops rapidly with sliding speed) could indeed allow, under certain conditions, for a pulse-like behavior of rupture to develop. Such models are supported by recent laboratory experiments with high sliding rates (*13*). However, simulations using velocity weakening have sometimes resulted in crack-like propagation or self-healing pulse-like propagation (*14*–*20*). Friction laws operating along faults that separate two identical elastic solids have to include laboratory-based rate and state evolution features (such as dependence on the slip rate and on the history of fault evolution), although these laws should not induce ill-posedness or paradoxical features (*20*) of the mathematical model of non-uniform sliding. It has been proven that generalized rate and state friction laws are appropriate candidates for modeling rupture in uniform faults (*20*–*22*). For rupture to occur as a self-healing pulse (*1*, *22*), three requirements have to be fulfilled. First, the friction law must include strengthening with time on slipped portions of the fault that are momentarily in stationary contact (*16*). Second, the velocity weakening at high slip rates must be much greater than that associated with the weak logarithmic dependence observed in the laboratory during low-velocity sliding experiments. Third, the overall driving stress has to be lower than a certain value but high enough to allow for self-sustained pulse propagation (*22*).

Strong velocity weakening may explain the onset of short-duration slip pulses along faults that separate similar materials. Other mechanisms exist as well. One mechanism (the barrier model) involves the geometric confinement of the rupture domain by unbreakable regions. In that case, an earthquake consists of a number of short-duration crack-like ruptures on a small rupture area that are separated by locked regions (*5*, *23*). Alternatively, the rupture may nucleate and propagate in both directions along the fault, while one of its tips arrests suddenly at a strong barrier in one side of the hypocenter. Consequently, after its arrest, the reflected waves from the barrier spread back and heal the rupture surface. In this case, the pulse-like configuration results from the interaction of the still-propagating end of the rupture with the healing reflected wave (*24*).

The variations in normal stress on the rupture interface are also thought to be responsible for pulse formation (*25*, *26*). As an example, the expansion of pore fluid, caused by frictional heating, may dramatically reduce the effective normal stress and consequently the frictional resistance. Pore pressure, however, may also rapidly decrease behind the rupture tip, causing a restrengthening and possibly a locking of the fault.

We performed a number of well-controlled experiments, all of which involved dynamic sliding along "incoherent" (frictional) interfaces separating identical materials (that is, homogeneous systems), to investigate the generation of the two rupture modes described above and to confirm the existence of pulse-like ruptures. Two plates of Homalite-100, subjected to a far-field uniform compressive stress, were frictionally held along the interface (or fault). The top plate was also subjected to dynamic shear loading. All the experiments were executed at the same external confining stress of P = 10 MPa, applied by a calibrated press. Dynamic photoelasticity, depicting the full-field contours of maximum shear stress, was combined with a laser interferometry–based technique, giving an accurate local measurement of the sliding velocity at the interface within an experimental error on the order of 1% (*27*). Detailed descriptions of the experimental configuration and the techniques used are provided in the supporting online material (SOM) (fig. S1).

In an instantaneous isochromatic fringe pattern obtained at an impact velocity V of 19 m/s (Fig. 1A), an eye-shaped fringe structure was observed traveling behind the longitudinal wavefront from right to left. The rupture tip A followed this fringe structure at a supershear speed of 1.36 C_S, where C_S is the shear wave speed of Homalite. Consequently, two Mach lines of shear stress discontinuity (*28*), forming a shear Mach cone, emanated from the sliding tip. The rupture tip speed v, which was obtained by two methods, was found to be constant. In the first method, the position of the tip was followed in various frames and found to be well approximated as a linear relation, giving v. In the second method, the Mach angle θ was measured and, by means of the relation $v = C_S/\sin\theta$ (*28*), v was obtained frame by frame.

The high-speed camera and both interferometers were simultaneously triggered. The synchronization of the 16 images captured by the high-speed camera, with the horizontal component of the local relative particle velocity recorded by the velocimeters, allowed the correlation of the characteristic features appearing in the photoelastic image (Fig. 1A) with the relative velocity history diagram (Fig. 1B). When the longitudinal wavefront arrived at the velocity measurement positions M_1 and M_2 (where the pair of the interferometric velocimeters was pointed), the velocities of both points started to increase. However, the relative horizontal velocity (Fig. 1B) was zero for the next few microseconds, and it remained very low for a time interval of approximately 13 μs. A numerical integration of the relative velocity with respect to time from 0 to 13 μs resulted in a net relative horizontal displacement of 2 μm between points M_1 and M_2 (fig. S4B). This observation is explained as an elastic shear deformation between M_1 and M_2, rather than rupture (interfacial sliding). The dashed line in Fig. 1B establishes the relative horizontal velocity level that corresponds to sliding initiation for this particular experiment. At approximately 13 μs, the relative velocity (Fig. 1B) rose sharply, and interfacial sliding began. After it reached its maximum of ~6 m/s, the relative velocity decreased and then fluctuated but never fell below 4 m/s during the recording time. The sliding was continuous, and thus we can safely say that rupture occurred in a classic crack-like mode. Additional details are provided in the SOM (figs. S3 and S4).

v was substantially higher than C_S, which resembles supershear rupture propagation occurring along "coherent" interfaces separating identical monolithic solids (*28*–*30*). However, in contrast to previous studies (*28*, *30*), the present work involves incoherent (or frictional) interfaces and a static far-field compressive loading. Here, the frictional resistance to sliding depends

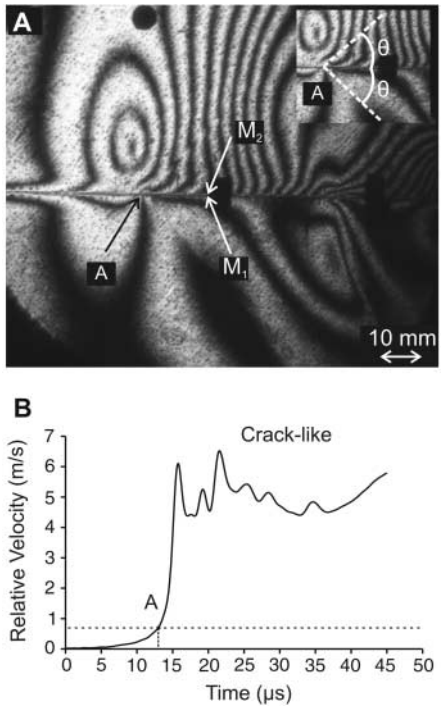

Fig. 1. (**A**) Isochromatic fringe pattern generated during an experiment in which the impact speed was 19 m/s. The rupture tip is at the fringe concentration point A. The inset highlights the location of the Mach lines emanating from the rupture tip and the specimen configuration. (**B**) Relative velocity history of points M_1 and M_2, which belong to the upper and lower plate, respectively; the two points are located at a distance of 70 mm from the impact side of the Homalite plates. The rupture commenced when the rupture tip A reached the velocity measurement position.

on the normal stress through the friction law. The fault-normal stress, however, is a superposition of the static externally imposed pressure and a dynamic (inertial) compression generated as follows: The pressure wave produced by the impact loading creates a primarily horizontal compressive stress in the upper plate close to the frictional interface. As a result of the Poisson effect (in which compression in the horizontal direction causes expansion in the vertical direction), the pressure wave also creates compression in the direction that is vertical to the interface. As the sliding proceeds, the vertical stress to the rupture interface changes, and thus the frictional resistance also changes. Consequently, we infer that sliding depends on impact loading, not only through the asymmetric horizontal compression, which is the driving force for sliding, but also through the vertical compression, which affects the resistance to sliding. Such dependence causes essential changes in the rupture modes that are expected to occur as the impact speed decreases.

Indeed, the reduction of the impact speed from 19 to 17 m/s resulted in drastic changes in the fringe pattern geometry (Fig. 2A). It also changed the horizontal relative velocity history of points M_1 and M_2 (Fig. 2B). By synchronizing the captured photoelastic frames with the horizontal relative velocity history, we were able to correlate the fringe concentration points A_1 and A_2 with abrupt changes in the horizontal relative velocity (Fig. 2B). At A_1, the relative velocity increased rapidly and the sliding started. This observation signifies that A_1 was the rupture tip. Thereafter, the relative velocity oscillated up to point A_3 (Fig. 2A), where the relative velocity increased and remained high for the rest of the recording time. The propagation speeds of A_1 and A_2 were 1.19 C_S and 1.0 C_S, respectively. Point A_3 propagated at a sub-Rayleigh speed of 0.85 C_S and signified the start of a clearly crack-like behavior of the rupture. Thus, it can be concluded that the event of rupture was constituted by two distinctive modes. From A_1 to A_3, the relative velocity changed twice, forming two pulses that were followed by a crack-like rupture mode that commenced at A_3.

By further decreasing the impact speed, a similar, albeit much simpler, behavior of the relative velocity was observed. Once again, we identified two rupture tips, A_1 and A_2, which were fringe concentration points and propagated along the rupture interface at speeds of 1.09 and 0.98 C_S, respectively (Fig. 2, C and D). The initial relative deformation at the velocity measurement position was elastic shear until approximately 18 μs, when the rupture tip A_1 arrived there and sliding commenced. As in the previous cases, the commencement of slip corresponded to an accumulated relative horizontal displacement of 2 μm. Subsequently, the horizontal relative velocity increased rapidly from 0.7 m/s to a local maximum of 2.5 m/s at 20 μs. After 5 μs, the relative velocity decreased abruptly back to 0.7 m/s at point A_2 (Fig. 2D). Because the relative velocity was very low, the slip ceased, allowing surface asperities to reestablish contact and be deformed elastically. Below the level established by the dashed line (Fig. 2D), we assume that there is no sliding and that the recorded velocity is only due to elastic shear deformation between points M_1 and M_2. This conjecture is strengthened by the relative displacement history (fig. S5B), which shows that, from 24 until 25 μs, the relative displacement was almost constant. These observations show that the stable fringe structure (A_1A_2) represents a self-healing slip pulse of ~7 μs in duration. Directly after the pulse, the relative velocity increased rapidly to 6.4 m/s and retained its large value of ~4 m/s for a relatively long period of time (~40 μs). The sliding velocity structure suggests that the initial rupture of the pulse-like mode was immediately followed by a second rupture of the crack-like mode. Thus, the experimental results indicate that the rupture process is very sensitive to impact speed. Indeed, as the impact speed was decreased while the external confining stress was kept constant, the rupture mode changed from a crack-like mode to a mixed mode, where either multiple slip pulses or a single self-healing slip pulse was followed by a crack.

The formation of pulses (Fig. 2) cannot be explained by the barrier model. A very simple calculation (fig. S2) reveals that these pulses were formed well before the arrival of the reflected waves (from the top and bottom hori-

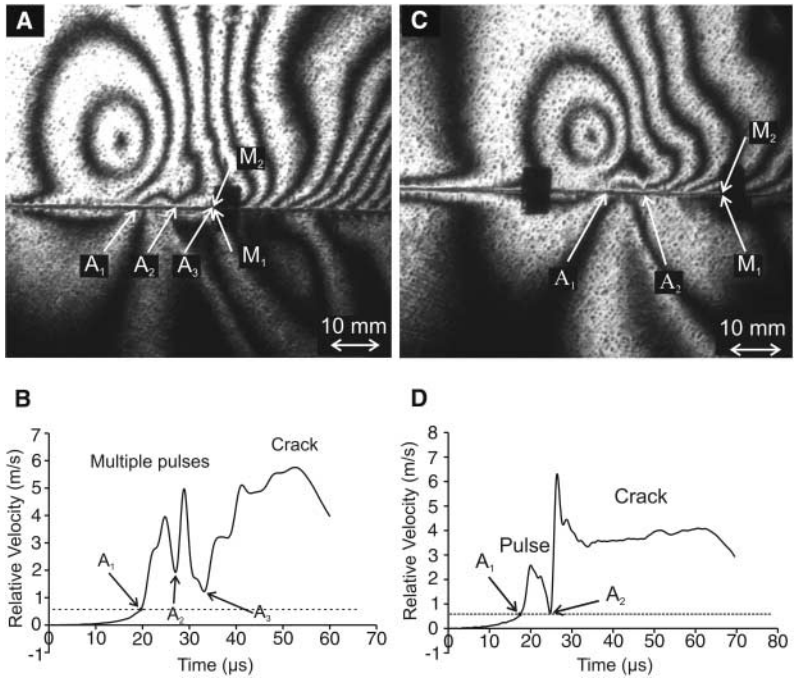

Fig. 2. (**A**) Isochromatic fringe pattern generated during an experiment in which the impact speed was 17 m/s. (**B**) Relative velocity history of points M_1 and M_2 located at a distance of 70 mm from the impact side of the Homalite plates. Two pulses, A_1A_2 and A_2A_3, were formed. The crack-like rupture mode initiated at A_3 immediately behind the second pulse. (**C**) Isochromatic fringe pattern generated during an experiment in which the impact speed was 13 m/s. (**D**) Relative velocity history of points M_1 and M_2 located at a distance of 30 mm from the impact side of the Homalite plates. A self-healing pulse A_1A_2 was formed. The crack-like rupture mode initiated at A_2 immediately behind the second pulse.

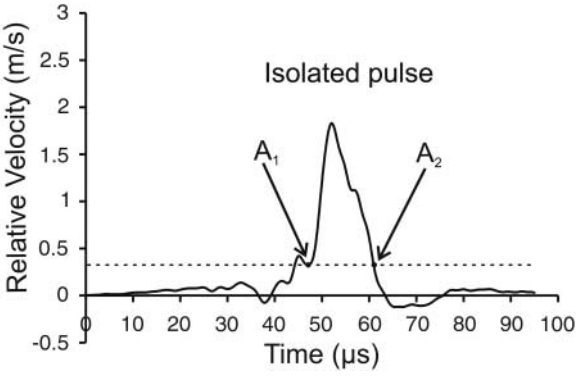

Fig. 3. Relative velocity history of points M_1 and M_2 for an experiment in which the impact speed was 10 m/s. M_1 and M_2 were located at a distance of 70 mm from the impact side of the Homalite plates. An isolated pulse A_1A_2 was formed.

zontal surfaces of the Homalite plates that were blocked by the hydraulic press) to the velocity measurement position. Also, the free surfaces (across the smallest dimension of the Homalite plates) did not act as barriers. We conjecture that the pulse formation was due either to the velocity-weakening character of the friction law or to the changes in the frictional resistance caused by non-uniform variations in dynamic normal stress on the rupture interface, or to a combination of both phenomena.

When the impact speed was further reduced to 10 m/s, the rupture mode became purely pulse-like (Fig. 3). The rupture started at A_1 and propagated at a sub-Rayleigh speed of 0.76 C_S, whereas, after 15 μs, the sliding ceased at A_2. The duration of sliding was very short compared to the ~100-μs duration of the impact event. Thus, we infer that an isolated pulse was formed. Such a case clearly indicates that a purely pulse-like mode of rupture can occur under the appropriate conditions.

References and Notes

1. J. R. Rice, in *Proceedings of the 20th International Congress of Theoretical and Applied Mechanics, 2000, Chicago*, H. Aref, J. W. Philips, Eds. (Kluwer Academic, Dordrecht, Netherlands, 2001), pp. 1–23.
2. A. J. Rosakis, *Adv. Phys.* **51**, 1189 (2002).
3. R. Madariaga, *Bull. Seismol. Soc. Am.* **66**, 639 (1976).
4. S. Das, K. Aki, *Geophys. J. Royal Astron. Soc.* **50**, 643 (1977).
5. S. M. Day, *Bull. Seismol. Soc. Am.* **72**, 705 (1982).
6. D. J. Andrews, *Bull. Seismol. Soc. Am.* **75**, 1 (1985).
7. R. A. Harris, S. M. Day, *J. Geophys. Res.* **98**, 4461 (1993).
8. T. H. Heaton, *Phys. Earth Planet. Inter.* **64**, 1 (1990).
9. S. H. Hartzell, T. H. Heaton, *Bull. Seismol. Soc. Am.* **73**, 1553 (1983).
10. H. L. Liu, D. V. Helmberger, *Bull. Seismol. Soc. Am.* **73**, 201 (1983).
11. S. Nielsen, R. Madariaga, *Bull. Seismol. Soc. Am.* **93**, 2375 (2003).
12. J. N. Brune, in *Seismic Risk and Engineering Decisions*, C. Lomnitz, E. Rosenbluth, Eds. (Elsevier, New York, 1976), pp. 141–171.
13. G. Di Toro, D. L. Goldsby, T. E. Tullis, *Nature* **427**, 436 (2004).
14. A. Cochard, R. Madariaga, *J. Geophys. Res.* **101**, 25,321 (1996).
15. N. M. Beeler, T. E. Tullis, *Bull. Seismol. Soc. Am.* **86**, 1130 (1996).
16. G. Perrin, J. R. Rice, G. Zheng, *J. Mech. Phys. Solids* **43**, 1461 (1995).
17. N. Lapusta, J. R. Rice, Y. Ben-Zion, G. Zheng, *J. Geophys. Res.* **105**, 23,765 (2000).
18. S. B. Nielsen, J. M. Carlson, K. B. Olsen, *J. Geophys. Res.* **105**, 6069 (2000).
19. D. Coker, G. Lykotrafitis, A. Needleman, A. J. Rosakis, *J. Mech. Phys. Solids* **53**, 884 (2005).
20. A. Cochard, J. Rice, *J. Geophys. Res.* **105**, 25891 (2000).
21. J. R. Rice, N. Lapusta, K. Ranjith, *J. Mech. Phys. Solids* **49**, 1865 (2001).
22. G. Zheng, J. R. Rice, *Bull. Seismol. Soc. Am.* **88**, 1466 (1998).
23. K. Aki, *J. Geophys. Res.* **84**, 140 (1979).
24. E. Johnson, *Geophys. J. Int.* **101**, 125 (1990).
25. E. Richardson, C. Marone, *J. Geophys. Res.* **104**, 28,859 (1999).
26. P. Bodin, S. Brown, D. Matheson, *J. Geophys. Res.* **103**, 29,931 (1998).
27. G. Lykotrafitis, A. J. Rosakis, G. Ravichandran, *Exper. Mech.* **46**, 205 (2006).
28. O. Samudrala, Y. Huang, A. J. Rosakis, *J. Geophys. Res.* **107**, 10129/2001JB000460 (2002).
29. A. Needleman, *J. Appl. Mech.* **66**, 847 (1999).
30. A. J. Rosakis, O. Samudrala, D. Coker, *Science* **284**, 1337 (1999).

31. The authors acknowledge the support of NSF (grant EAR 0207873) and the U.S. Department of Energy (grant DE-FG52-06NA26209). The consistent support of the Office of Naval Research through grant N00014-03-1-0435 (Y. D. S. Rajapakse, Program Manager) is also gratefully acknowledged. The authors also thank H. Kanamori, A. Needleman, D. Coker, and N. Lapusta for their many constructive suggestions.

Supporting Online Material

www.sciencemag.org/cgi/content/full/313/5794/1765/DC1
Materials and Methods
Figs. S1 to S5
Reference

5 April 2006; accepted 26 July 2006
10.1126/science.1128359

Observations of Biologically Generated Turbulence in a Coastal Inlet

Eric Kunze,[1]* John F. Dower,[1]* Ian Beveridge,[2] Richard Dewey,[1] Kevin P. Bartlett[1]

Measurements in a coastal inlet revealed turbulence that was three to four orders of magnitude larger during the dusk ascent of a dense acoustic-scattering layer of krill than during the day, elevating daily-averaged mixing in the inlet by a factor of 100. Because vertically migrating layers of swimming organisms are found in much of the ocean, biologically generated turbulence may affect (i) the transport of inorganic nutrients to the often nutrient-depleted surface layer from underlying nutrient-rich stratified waters to affect biological productivity and (ii) the exchange of atmospheric gases such as CO_2 with the stratified ocean interior, which has no direct communication with the atmosphere.

Turbulent mixing in the ocean plays key roles in a wide range of processes, from regulating the large-scale thermohaline overturning circulation (also known as the global conveyor belt) and water-mass modification, to the dispersal and dilution of anthropogenic waste. Below the surface mixed layer, turbulent mixing controls the exchange of water properties between the surface layer, which is in direct contact with the atmosphere, and the density-stratified ocean interior, where mixing is typically reduced to diffusivities on the order of 0.1×10^{-4} m^2 s^{-1} (*1*, *2*), controlled by the breaking of internal waves generated by the wind and tides. Exchange across the highly stratified base of the surface mixed layer influences not only biological productivity through nutrient supply but also air/sea gas exchange (*3*). By providing another mechanism by which nutrients and tracers can pass between the nutrient-limited surface mixed layer and the underlying nutrient-replete stratified ocean, biologically generated turbulence could (i) explain how surface production is often higher than can be accounted for by known mixing mechanisms (*4*) and (ii) regulate gas exchange between the ocean and atmosphere, which plays a key role in the carbon cycle, carbon sequestration, and climate.

Although marine organisms have long been known to be capable of generating turbulence (*5*–*8*), the role of biologically generated turbulent mixing in the ocean has largely been neglected, perhaps because this mechanism was discounted in earlier work (*9*). However, more recent evaluations based on the energetics of swimming organisms suggest that species ranging in size from large zooplankton (0.5 cm) to cetaceans on the order of 10 m long can generate turbulent dissipation rates ε (the rate at which turbulent kinetic energy is damped by molecular viscosity) on the order of 10^{-5} W kg^{-1} within schools and swarms (*10*, *11*). Such high values, fully three to four orders of magnitude larger than average turbulence levels in the stratified ocean, have the potential to dominate mixing in the upper ocean, where marine organisms are most abundant. Here we report observations quantifying biologically generated turbulence in a coastal inlet.

The above notion was tested by collecting microstructure profiles with depth during dusk in Saanich Inlet, British Columbia. The profiler measures microscale (1 cm) shear, temperature, and conductivity, as well as fine-scale (1 m) temperature, conductivity, and pressure. Profiles were collected at 3-min intervals. Microscale shear measurements were de-spiked before processing to remove plankton collisions. Following common practice, dissipation rates were estimated by iteratively fitting shear spectra from 4-m half-overlapping profile segments to a turbulence model spectrum (*12*). The wavenumber band from 1 to 100 cpm (wavelengths of 0.01 to 1 m) was typically fit for dissipation rates exceeding 10^{-7} W kg^{-1}. A shipboard 200-kHz ASL Environmental Sciences Water Column Profiler single-beam echosounder (*13*)

[1]School of Earth and Ocean Sciences, University of Victoria, Post Office Box 3055, STN CSC Victoria, BC, V8W-3P6, Canada. [2]Department of Biology, University of Victoria, Post Office Box 3020, STN CSC Victoria, BC, V8W-3N5, Canada.

*To whom correspondence should be addressed. E-mail: kunze@uvic.ca (E.K.); dower@uvic.ca (J.F.D.)